Supporting Information for
"3D Relaxation-Assisted Separation of Wideline Solid-State NMR Patterns for Achieving Site Resolution"

Adam R. Altenhof[1,2], Michael J. Jaroszewicz[3], Lucio Frydman[2,3,*], and Robert W. Schurko[1,2,*]

1. Department of Chemistry and Biochemistry, Florida State University, Tallahassee, FL 32306, USA
2. National High Magnetic Field Laboratory, 1800 East Paul Dirac Drive, Tallahassee, FL 32310, USA
3. Department of Chemical and Biological Physics, Weizmann Institute of Science, Rehovot, Israel, 7610001

*Author to whom correspondence should be addressed.
Phone: (850)-645-8614, E-mails: rschurko@fsu.edu, lucio.frydman@weizmann.ac.il

Table of Contents:

Table S1: Experimental Parameters for ^{35}Cl WCPMG-IR Experiments in **Fig S1** and **Fig 4**.

Number of Transients	340
IR delays (τ)	32 points between 0.001 and 7 s
Recycle Delay (s)	7
Spectral Window Width (kHz)	500
Dwell Time (μs)	2
Number of Meiboom-Gill loops (*N*)	94
Spin Echo Length (μs)	400
Acquisition Time (ms)	48.3
WURST-A length (ms)	5
WURST-A Sweep width (kHz)	500
WURST-A Amplitude (kHz)	27.5
WURST-B length (μs)	50
WURST-B Sweep width (kHz)	500
WURST-B Amplitude (kHz)	16

Table S2: Experimental Parameters for ^{2}H QCPMG-IR Experiments in **Fig 2** and **Fig 7**.

Number of Transients	512
IR delays (τ)	32 points between 0.001 and 3 s
Recycle Delay (s)	3
Spectral Window Width (kHz)	1000
Dwell Time (μs)	1
Number of Meiboom-Gill loops (*N*)	64
Spin Echo Length (μs)	700
Acquisition Time (ms)	31.2
Excitation Pulse Width (μs)	2.5
Refocusing Pulse Width, τ_{ref} (μs)	1.00
Excitation Pulse Power, ν_{exc} (kHz)	100
Refocusing Pulse Power, ν_{ref} (kHz)	100

Table S3: Experimental Parameters for ^{35}Cl WCPMG-IR Experiments in **Fig 5**.

Number of Transients	1024
IR delays (τ)	32 points between 0.001 and 3 s
Recycle Delay (s)	3
Spectral Window Width (kHz)	500
Dwell Time (μs)	2
Number of Meiboom-Gill loops (*N*)	85
Spin Echo Length (μs)	300
Acquisition Time (ms)	31.7
WURST-A length (ms)	5
WURST-A Sweep width (kHz)	400
WURST-A Amplitude (kHz)	25
WURST-B length (μs)	50
WURST-B Sweep width (kHz)	400
WURST-B Amplitude (kHz)	12.3

Table S4: Experimental Parameters for ^{35}Cl WCPMG-IR Experiments in **Fig 6**.

Number of Transients	350
IR delays (τ)	32 points between 0.01 and 6 s
Recycle Delay (s)	6
Spectral Window Width (kHz)	1000
Dwell Time (μs)	1
Number of Meiboom-Gill loops (*N*)	200
Spin Echo Length (μs)	350
Acquisition Time (ms)	82.5
WURST-A length (ms)	1
WURST-A Sweep width (kHz)	700
WURST-A Amplitude (kHz)	24.9
WURST-B length (μs)	50
WURST-B Sweep width (kHz)	700
WURST-B Amplitude (kHz)	19.9

Table S5: Experimental Parameters for ^{14}N BRAIN-CP-IR Experiments in **Fig 8**.

Number of Transients	1024
IR delays (τ)	32 points between 0.1 and 12 s
Recycle Delay (s)	1
Spectral Window Width (MHz)	1.8727
Dwell Time (μs)	0.534
Number of Meiboom-Gill loops (*N*)	120
Spin Echo Length (μs)	150
Acquisition Time (ms)	29.3
^{1}H Excitation Pulse Length (μs)	3.125
^{1}H Excitation Pulse Amplitude (kHz)	80
^{1}H CP Pulse Amplitude (kHz)	50
CP Contact Time (ms)	10
†WURST-A Amplitude (kHz)	34.9
WURST-A Sweep width (kHz)	1300
WURST-B length (μs)	50
WURST-B Sweep width (kHz)	1300
WURST-B Amplitude (kHz)	29.3

†All WURST-A and WURST-B pulses in the sequence are swept from low-to-high frequency and the center offset of the sweep is set to +139 kHz with respect to $\upsilon_0(^{14}N)$.

Table S6: Fitted EFG Tensor Parameters and Isotropic Shifts for ^{35}Cl spectra in **Fig 6**.

Site	C_Q (MHz)[a]	η_Q[b]	δ_{iso} (ppm)[c]
1	12.1	0.15	130
2	5.4	0.35	177
3	4.0	0.92	170

[a] $C_Q = eQV_{33}/h$. [b] $\eta_Q = (V_{11} - V_{22})/V_{33}$. [c] $\delta_{iso} = (\delta_{11} + \delta_{22} + \delta_{33})/3$.

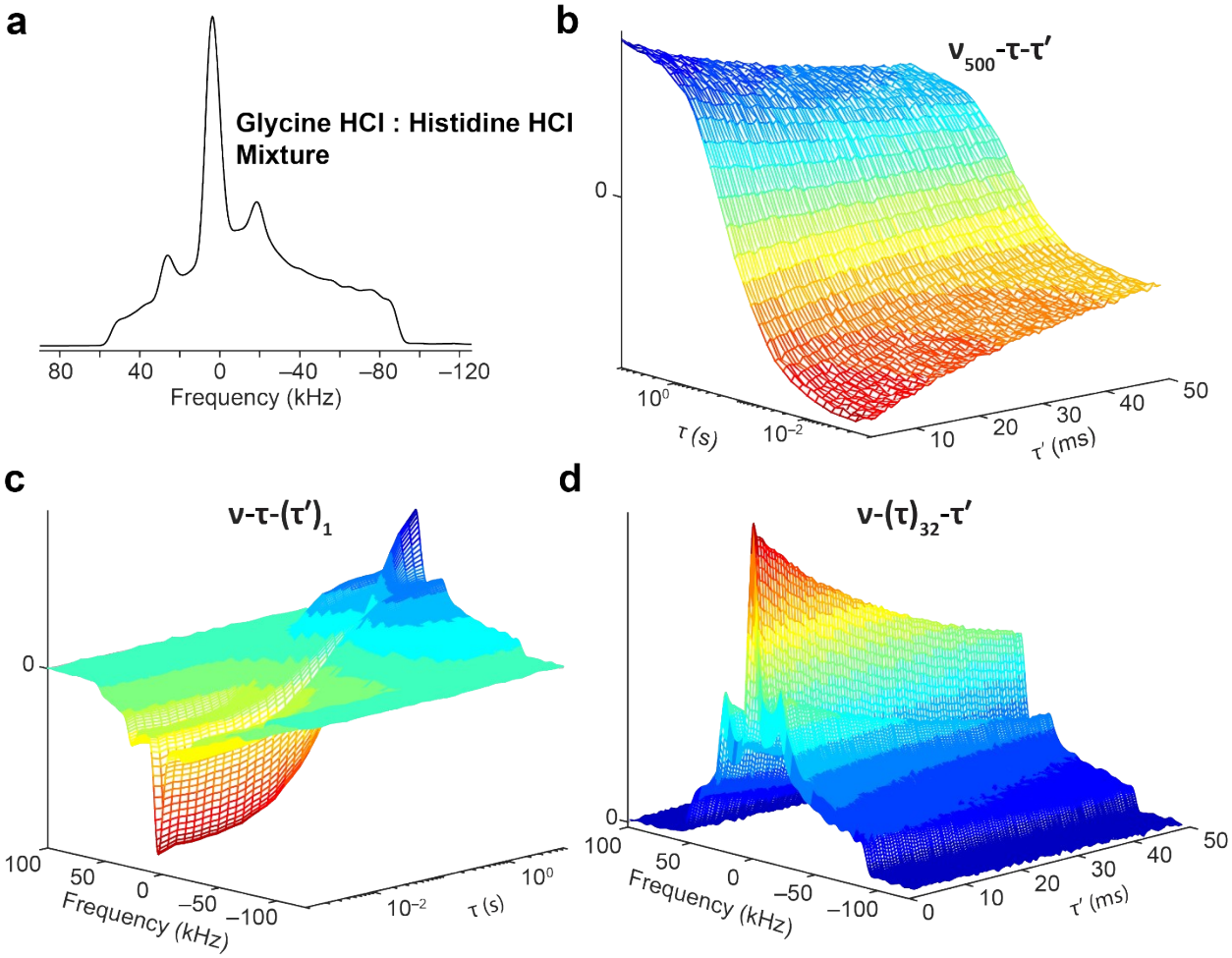

Figure S1: (a) An experimental 1D ^{35}Cl NMR spectrum of a glycine HCl:histidine HCl 3:1 w/w mixture. The corresponding 3D WCPMG-IR data of the mixture can be visualized with (b) a 2D τ-τ′ slice at the 500th frequency point in the spectrum (corresponding to the signal at *ca.* +5 kHz in (a)), (c) a 2D ν-τ slice for the first spin echo in the windowed CPMG acquisition, and (d) a 2D ν-τ′ slice for the last inversion recovery increment (the 32nd τ increment).

Discussion of Figure S1

An example of the T_1-T_2 encoding using WCPMG-IR (**Scheme 1**) is shown for the ^{35}Cl NMR of a glycine HCl:histidine HCl 3:1 w/w mixture (**Figure S1**). Glycine HCl has a broad ^{35}Cl CT powder pattern with a breadth of *ca.* 160 kHz at 14.1 T, whereas histidine HCl has a much narrower pattern that spans *ca.* 20 kHz; therefore, both patterns are distinguishable in the 1D spectrum (**Figure S1a**). The simultaneous relaxation decay processes arising from IR and CPMG

can be visualized for a single frequency point (an example is shown for the 500th frequency point in the spectrum, ν_{500}, which approximately corresponds to the middle of the pattern, **Figure S1b**). This representation corresponds to the 2D input $G_k(\tau,\tau') = \mathbf{S}_k$ that is compressed with TSVD yielding $\tilde{\mathbf{S}}_k$, then vectorized into $\tilde{\mathbf{s}}_k$, and then solved according to the Eq. 11. Representations of the ν-τ (**Figure S1c**) or ν-τ′ (**Figure S1d**) encodings appear as standard IR or CPMG datasets, respectively. Either of these latter datasets can be used as input for 2D R_1- or R_2-RAS that was previously described by our research group, where the input is also rearranged to vectors and the Sparse NNTF routine is also used individually for every frequency point, k.[1]

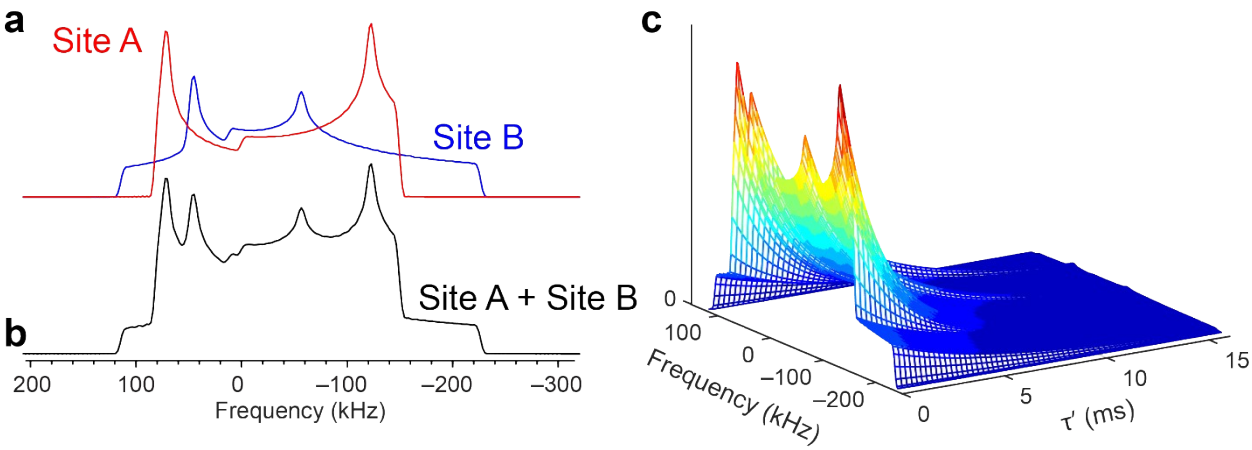

Figure S2: (a) Simulated ^{35}Cl NMR powder patterns with EFG tensor parameters of C_Q = 9.8 MHz and η_Q = 0.1 for site A and C_Q = 10 MHz and η_Q = 0.6 for site B simulated at 14.1 T and (b) the sum of the two spectra. (c) Synthetic CPMG data showing R_2 decay of the patterns where a unique R_{2A} and R_{2B} is applied for either site.

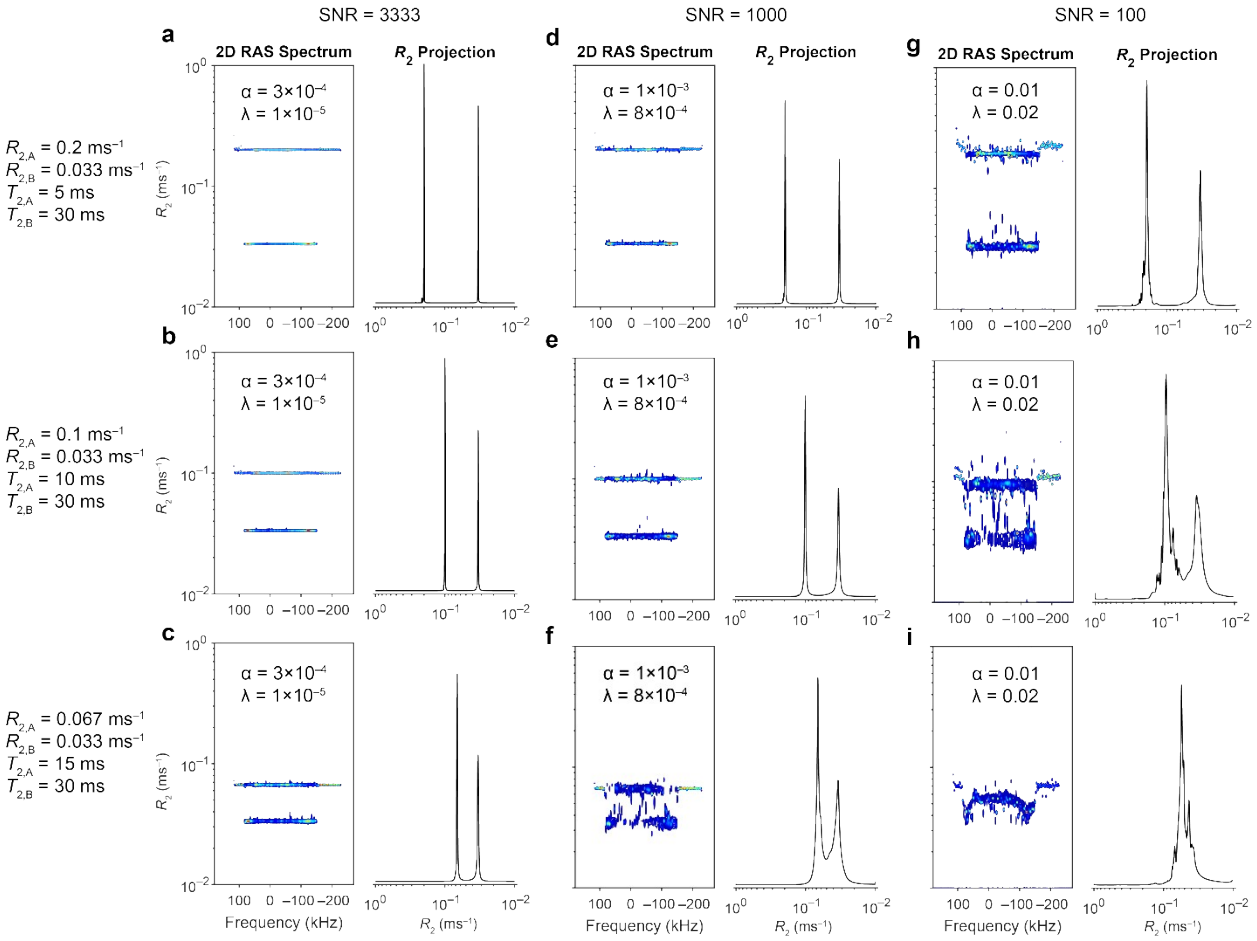

Figure S3: 2D R_2 RAS of simulated nonequivalent ^{35}Cl powder patterns using synthetic CPMG data. Each column shows the 2D RAS frequency-R_2 contour spectrum and a projection of the corresponding 1D R_2 dimension. Each column has a different signal-to-noise ratios (SNR) of the input data. Each row has a unique combination of applied rates $R_{2,A}$ ($T_{2,A}^{-1}$) and $R_{2,B}$ ($T_{2,B}^{-1}$). In every case (a – i) the regularization parameters used for RAS are noted as α and λ for the l_2 and l_1 norm constraints, respectively.

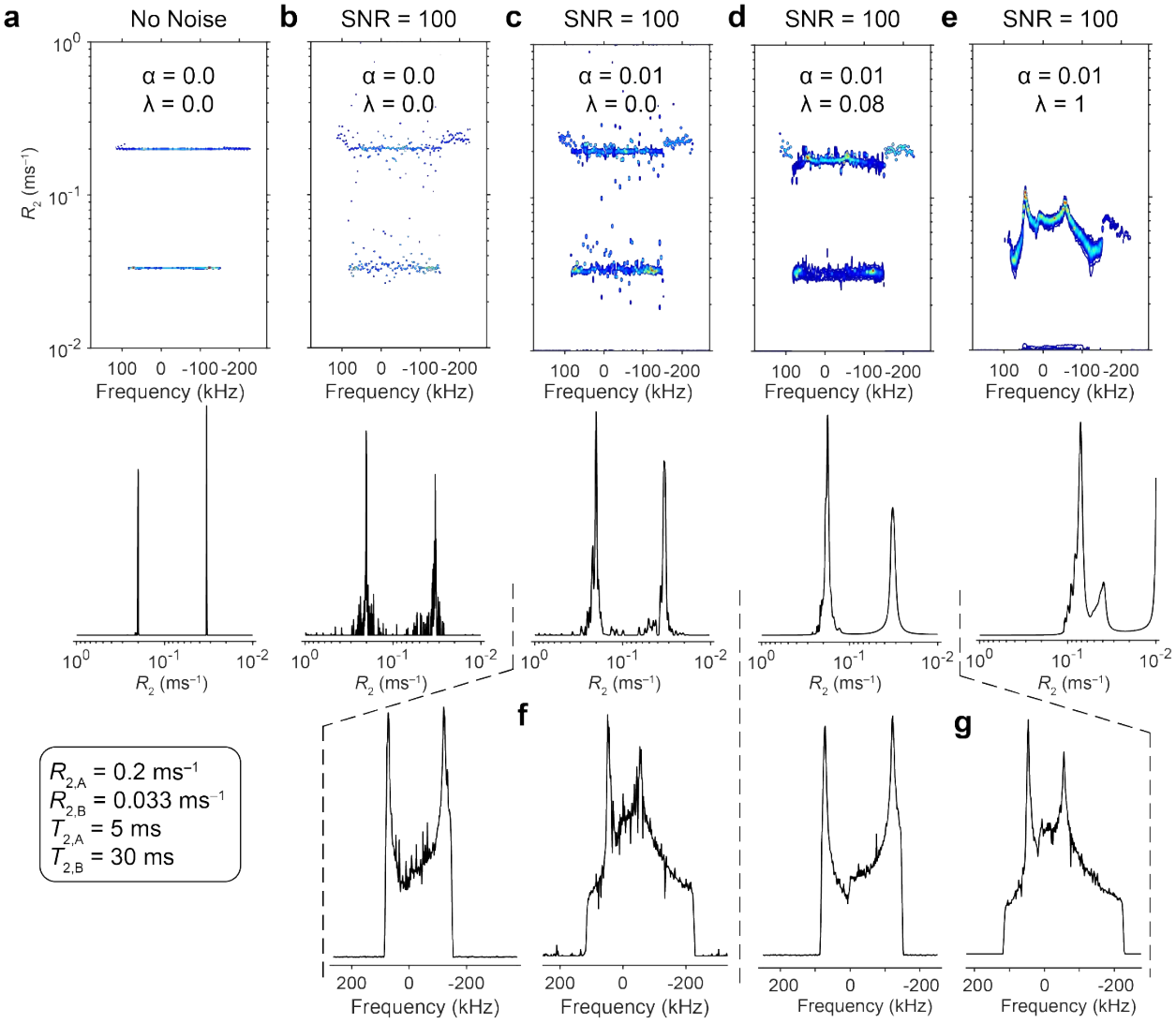

Figure S4: 2D R_2 RAS of simulated nonequivalent ^{35}Cl powder patterns using synthetic CPMG data. In each column the RAS spectrum is shown with its corresponding 1D R_2 projection below it for: (a) no noise or regularization; (b) added noise and no regularization; and (c)-(e) added noise, a fixed amount of l_2 regularization (α), and an increasing amount of l_1 regularization (λ). (c) In the absence of l_1 regularization there are many spurious rates and artifacts between the two main distributions. (d) Two distinct rate distributions are identifiable with minor artifacts when using an optimal λ that was empirically determined. (e) When λ is too large either rate distribution starts to significantly overlap with one another making it difficult to separate either powder pattern. Projections of the powder patterns from either rate distribution when (f) λ = 0 and (g) when using an optimal λ. The optimal λ can be determined with a characteristic S-curve plotting routine (*vide infra*) and be can further refined if *a priori* knowledge of the separated pattern shapes are known.

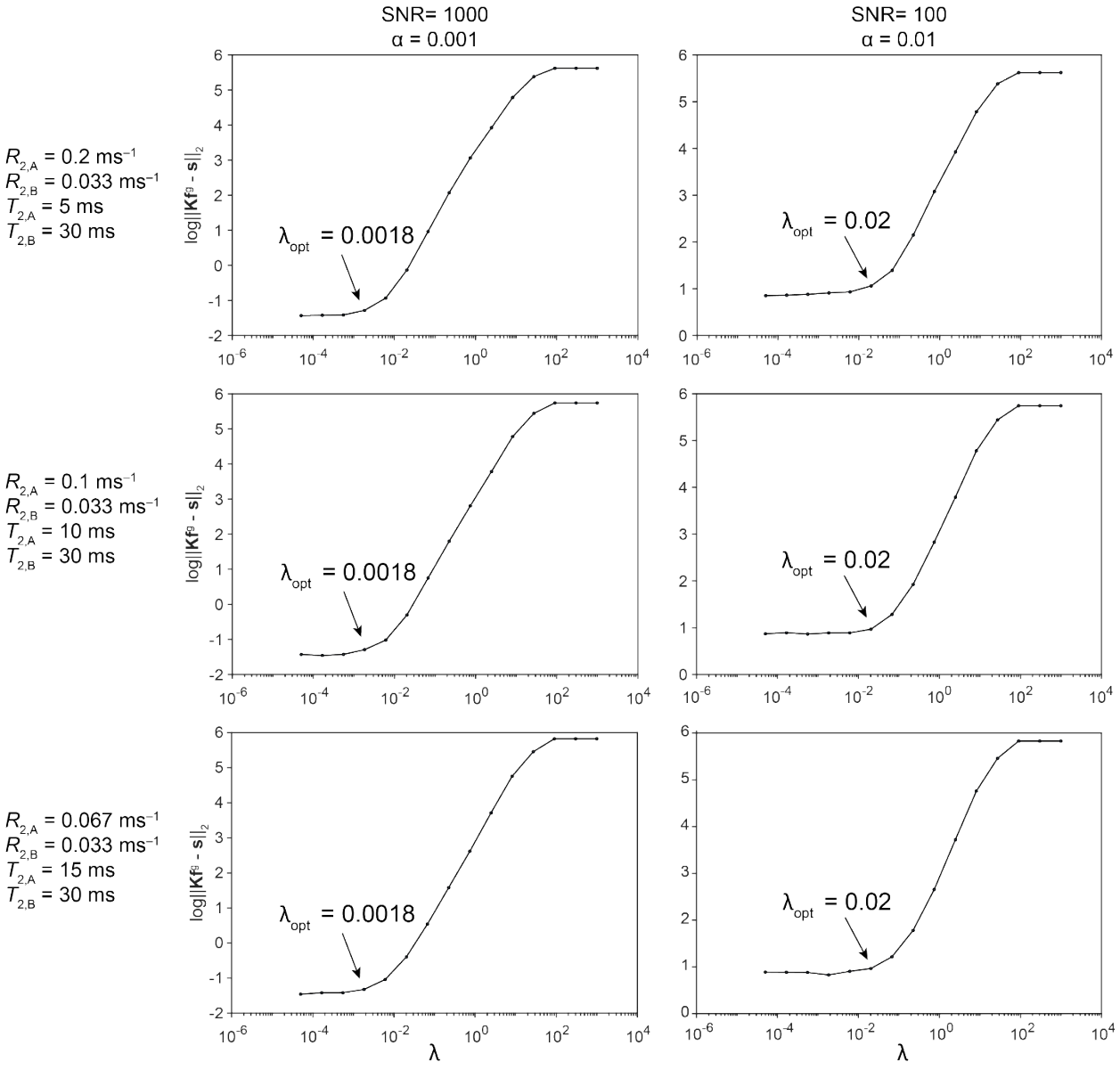

Figure S5: Examples of the S-curve plotting routine used to determine an optimal l_1 norm constraint, λ. In each plot, the vertical axis is the log of the residual norm after Sparse NNTF and the horizontal axis represents different values of λ. The plot depicts a characteristic 'S' shape where the first corner of the S represents an approximate value for the optimal λ.[2,3] This value can be further refined empirically (*cf.* **Figure S4**) for optimal pattern separation if needed. Examples are given corresponding to 2D R_2 RAS simulations shown in **Figure 1**. Each column represents different levels of SNR and l_2 norm constraints (α), while each row represents different rates used as input for each site used in the simulation.

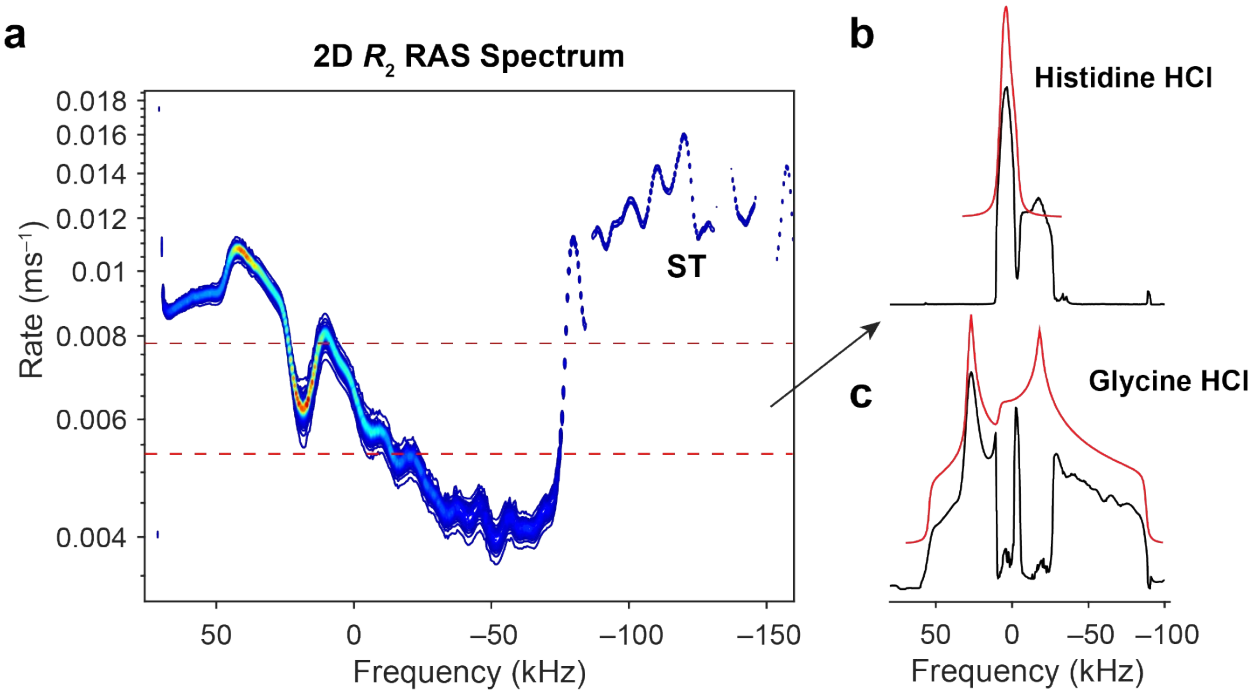

Figure S6: (a) Experimental 2D R_2 RAS spectrum of a glycine HCl: histidine HCl 3:1 w/w mixture using ^{35}Cl NMR with regularization parameters $\alpha = 0.001$ and $\lambda = 0.00005$. Signal below *ca.* –90 kHz is from the satellite transitions (STs). (b) Frequency projection from summing over the rates between the dashed red lines and (c) a frequency projection from summing over the rates outside of the dashed red lines. Ideal ^{35}Cl NMR patterns are simulated for each pattern. The R_2 of glycine HCl has a large distribution across isochromats such that it is completely overlapped with the small R_2 distribution of histidine HCl. The overlapping R_2 distributions between the samples makes it challenging to separate the patterns without major distortions.

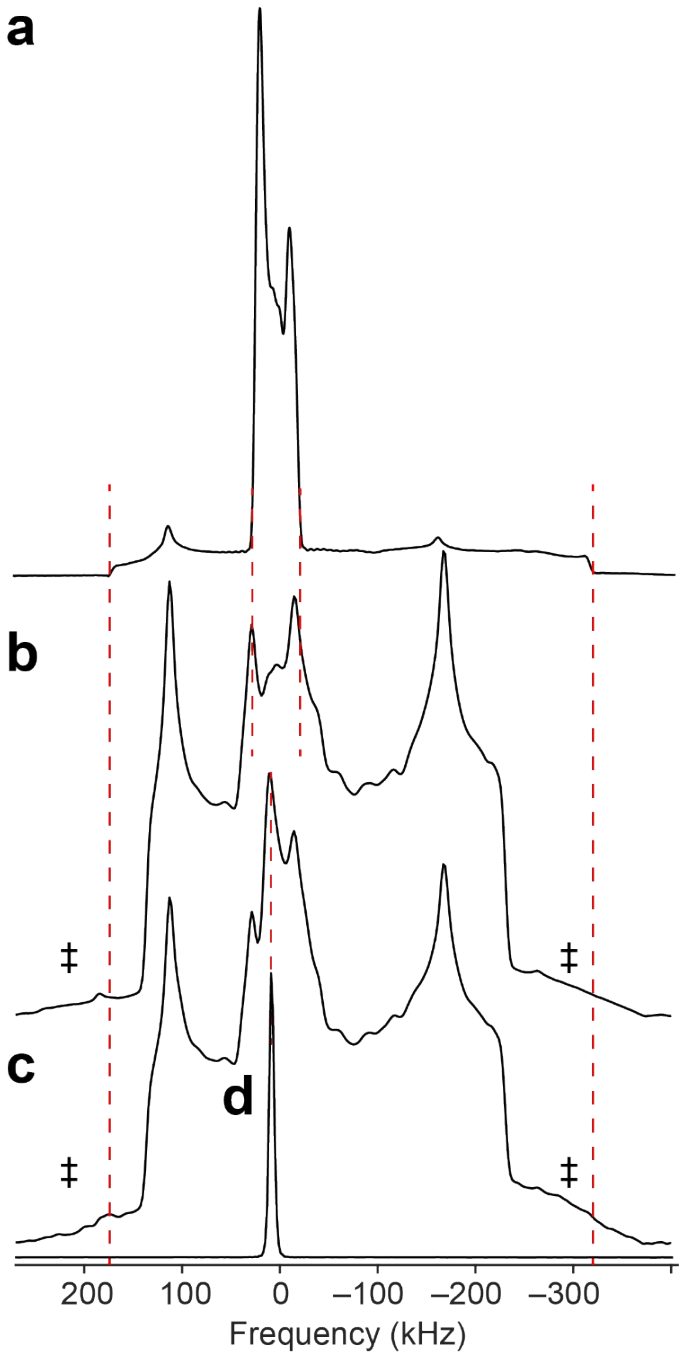

Figure S7: Experimental ^{35}Cl WURST-CPMG NMR spectra of (a) $CdCl_2$, (b) the RbCl:$CdCl_2$:Urea cocrystal processed by coadding all 200 echoes and (c) processed by coadding just the first 10 echoes, and (d) a Bloch decay spectrum of RbCl. $CdCl_2$ has one broad and one narrow ^{35}Cl powder pattern. The broad pattern in (a) is unique from the broad pattern in the cocrystal as indicated by the broad red dashed lines between (a), (b), and (c). The narrow pattern in (a) is also unique from the narrow pattern in the cocrystal as indicated by the narrow-dashed lines between (a) and (b). Both comparisons suggest that the cocrystal is a novel material and contains little or no $CdCl_2$ starting reagent. A distinct narrow ^{35}Cl resonance is distinguishable in (c) compared to (b), suggesting that this narrow pattern has a much shorter T_2 compared to that

of the broader sites. A red dashed line between RbCl in (d) and the narrowest pattern in (c) suggests this narrowest pattern in the cocrystal may correspond to residual RbCl from synthesis. ‡ indicates a broad resonance in (b) and (c) that cannot be distinguished as another CT pattern or STs and extends well beyond the tuning range of the probe (*c.f.* **Figure S8**).

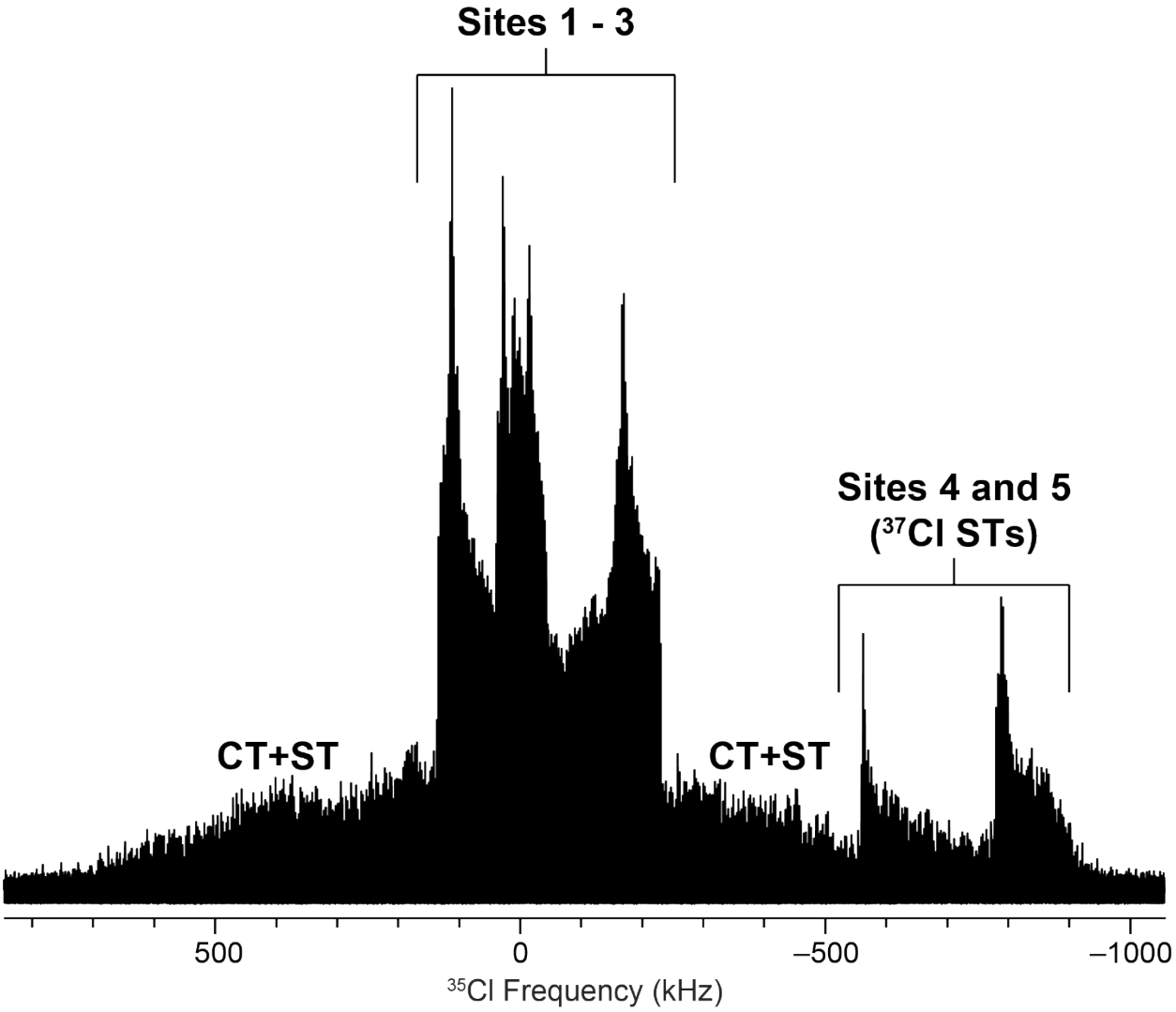

Figure S8: Experimental ^{35}Cl NMR of the RbCl:$CdCl_2$:Urea cocrystal acquired with WURST-CPMG. The spectrum was acquired with two different sub-spectra at transmitter offsets of ± 350 kHz with respect to $\nu_0(^{35}Cl)$. These offsets are at the tuning limits of the probe and the spectrum cannot be acquired beyond this range. The patterns of the three Cl sites described in **Figure S7** are denoted as **Sites 1-3**. Signal corresponding to ^{37}Cl STs associated with two additional Cl sites (**4 and 5**) are clearly noticeable and suggest C_Q values greater than *ca*. 30 MHz; therefore, corresponding CT ^{35}Cl powder patterns for **4 and 5** span well beyond the current acquisition bandwidth and likely also overlap with ^{35}Cl ST signal for **Sites 1-3**.

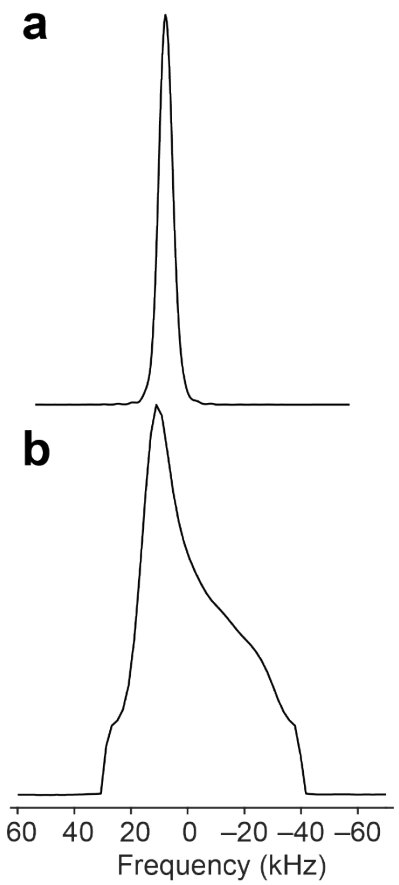

Figure S9: Experimental ^{35}Cl NMR of (a) RbCl and (b) the pattern of **Site 3** extracted from the 3D RAS R_1-R_2 correlation map in **Figure 6d**. A qualitative comparison of these patterns suggests that **Site 3** extracted from the R_1-R_2 correlation map for the RbCl:$CdCl_2$:Urea cocrystal is not residual RbCl from synthesis, and is a novel ^{35}Cl site within the cocrystal.

References

(1) Jaroszewicz, M. J.; Frydman, L.; Schurko, R. W. *J. Phys. Chem. A* **2017**, *121*, 51–65.

(2) Song, Y.-Q.; Venkataramanan, L.; Hürlimann, M. D.; Flaum, M.; Frulla, P.; Straley, C. *J. Magn. Reson.* **2002**, *154*, 261–268.

(3) Guo, J.; Macmillan, B.; Zamiri, S.; Balcom, B. *J. Magn. Reson.* **2021**, 107005.